IEEE Access
Multidisciplinary | Rapid Review | Open Access Journal

Received September 28, 2020, accepted October 8, 2020, date of publication October 14, 2020, date of current version October 27, 2020.

Digital Object Identifier 10.1109/ACCESS.2020.3030878

Monitoring Water Quality Parameters of Taihu Lake Based on Remote Sensing Images and LSTM-RNN

CHUHAN QI, SHUO HUANG, AND XIAOFEI WANG
College of Electronic Engineering, Heilongjiang University, Harbin 150080, China
Corresponding author: Xiaofei Wang (nk_wxf@hlju.edu.cn)

This work was supported in part by the National Natural Science Foundation of China under Grant 61871150, and in part by the National Key Research and Development Program of China under Grant 2016YFB0502502.

ABSTRACT Long-term dynamic monitoring of the water quality of freshwater resources is of great significance to the stable and orderly operation of human society. Most studies only use one of the measured data from the monitoring station and the remote sensing satellite data as the data source. However, a single data source will cause inaccuracy and incompatibility of the water quality monitoring results. Few studies start from practical applications to generate digital images of water quality changes. Furthermore, the performance of shallow neural networks in water quality monitoring is not often ideal. Considering the above problems, we proposed a long short-term memory network model (LSTM) to invert four key water parameters including pondus hydrogenii (PH), dissolved oxygen (DO), chemical oxygen demand (COD_{Mn}) and ammonia-nitrogen (NH_3-H). Moreover, the model was applied to the satellite images of various periods to generate the inverted image of each water quality parameter. The proposed model has exhibited excellent performance in the water quality assessment of the project, with the coefficient of determination (R^2), the relative root-mean-square error (rRMSE), and the mean relative error (MRE) values of 0.83, 0.16, and 0.18, respectively. And the inverted images are also consistent with the official information.

INDEX TERMS Remote sensing, water quality parameters, water quality monitoring, LSTM network.

I. INTRODUCTION

Adequate and high-quality water is one of the most important foundations for the healthy and sustainable development of human society and ecosystems [1]. Water quality is broadly defined as the biological, chemical, and physical characteristics of water to be maintained to meet the needs of various water usages including drinking, irrigation, and recreation [2]. As the largest developing country in the world, many parts of China face severe water stress as well as the health risks caused by water contamination, after ever-growing demands and misuse of surface water resources over the last decades [3]. In order to meet the needs of water for human life, industrial production and agricultural irrigation, it is urgent to propose an efficient and convenient method for long-term dynamic monitoring of water quality.

In recent years, calculating the water quality parameter is used widely as a tool to classify and characterize water resources for different activities such as agriculture and drinking purposes among many others [4]. However, since different water quality parameters have different limitations in specific research, more studies have focused on the efficient approaches for determining key water quality parameters and measuring and analyzing them at low cost [5]. Mohammadmehdi *et al.* developed a semi-empirical model for predicting Chl-a and Total Suspended Solids (TSS) by combing Sentinel-2A data and machine learning using samples collected from several water reservoirs within the southern part of the Czech Republic, Central Europe. The results showed that the model performed well for both Chl-a ($R^2 = 0.85$) and TSS ($R^2 = 0.80$) [6]. Under the ice-free condition, Griffin *et al.* used Landsat TM and ETM+ data to invert the colored dissolved organic matter (CDOM) and dissolved organic carbon in major Arctic rivers, and the R^2 reached 0.67 to 0.84 [7]. Chen *et al.* developed an empirical band ratio algorithm using the model ranking method to determine the best band ratio as well as their empirical functions, and derived a CDOM that could be directly applied to Landsat-8 imagery, which demonstrated the potential applications of estimating CDOM from Landsat-8 imagery

The associate editor coordinating the review of this manuscript and approving it for publication was Andrea F. Abate.

in long-term and large-scale water quality monitoring [8]. In order to fully understand the temporal-spatial changes of water quality, Xia *et al.* collected monthly data of 8 water quality parameters of the Three Gorges Reservoir after its experimental impoundment. By analyzing the water quality status and trends, they finally concluded that most water quality parameters showed obvious seasonal patterns [9]. However, the performance of the model of water quality parameter inversion needs to be carefully considered and evaluated in combination with the specific research background [10].

In regard to hydrological monitoring, a great number of environmental monitoring data have traditionally been collected worldwide by individual environmental departments and agencies [11]. The four key water quality parameters selected in this study, including PH, DO, COD_{Mn} and NH_3-H, and water quality classification standards are all adopted from the China National Environmental Monitoring Centre. PH is an index reflecting the acidity and alkalinity of water, which not only directly affects the physiological activities of aquatic organisms, but also indirectly affects human beings by changing the physicochemical and biological factors in the water environment [12]. The PH of the water suitable for the general production and living needs of human beings should be within the range of [7.5, 8.5], beyond which the water body may be polluted. DO is molecular oxygen dissolved in the air in water, and its content is an indicator to measure the self-purification ability of the water body. After the DO in the water is consumed, if it returns to the initial state in a short time, it indicates that the water body has a strong self-purification capacity, or that the water body is not seriously polluted. According to China's regulations on ground water quality standard, the DO content in the water should be not less than 4 mg/L (level III) [13]. NH_3-H refers to nitrogen in the form of free ammonia (NH_3) and ammonium ions (NH_4^+) in water. Free ammonia, also known as non-ionic ammonia, is the leading factor causing toxicity to aquatic organisms, while ammonium ions are relatively non-toxic. When oxygen-consuming organisms in water increase, DO decreases accordingly, resulting in an increase in the content of NH_3-H in the water, which in turn affects the PH of the water [14]. COD_{Mn} is a chemical method to measure the amount of reductive substances that need to be oxidized in a water sample. It is an important and fast determination of organic pollution parameters [15]. The determination method of COD_{Mn} in this study is the acid potassium permanganate oxidation (K_2MnO_4) method, which is widely used at present. Although the oxidation rate of this method is lower, the actual operation is relatively more convenient and efficient.

Since 1970, remote sensing technology has gradually been applied from ocean water color remote sensing to the study of inland water, from simple water identification to remote sensing monitoring of water quality parameters. Water absorbs radiation in the red and near-infrared regions of the electromagnetic spectrum, and no reflectance signal is detectable from a clear body of water from the wavelength 750 nm or longer [16]. Long-term monitoring of water quality using remote sensing techniques benefits from observation complementarities and synergies by combining in-situ measurements and satellite images to provide more precise and higher temporal resolution monitoring [17]. Remote sensing satellites have been used by researchers to observe water quality changes due to their various advantages. Francis *et al.* used satellite data to observe water quality changes from the northern Bay of Biscay to the eastern of the English Channel over a period of 20 years [18].

Medium spatial resolution sensors (10 to 30m) designed for terrestrial mapping are capable of resolving approximately 90% or more of global lake area and their radiometric sensitivity has been improving with advancing technology [19]. Landsat-8 has been applied to inland water monitoring due to increased spectral sampling and radiometric performance advances over its predecessors [20]. Additional improvements to spectral resolution and spectral sampling of Landsat sensors should enhance monitoring of complex inland waterbodies [21]. However, the potential risk of augmented spectral sampling affecting Landsat data continuity must be considered [22]. Therefore, Landsat-8 remote sensing data is used in this study.

Machine learning for remotely sensed water quality estimation has become popular in recent years thanks to the advances in algorithm development, computing power, sensor systems, and data availability [23]. The most powerful form of machine learning is so called deep learning (DL), a hierarchically structured neural network that can extract useful information and make predictions from raw data. DL has shown unparalleled advantages for water quality mapping [24]. Since 2014, the remote-sensing community has shifted its attention to DL, and DL algorithms have achieved significant success at many tasks including land use [25] and land cover classification [26], equipment fault detection [27], scene classification [28], and object detection [29]. As an alternative widely used supervised learning model, the recurrent neural network (RNN) model is traditionally used for a discrete sequence analysis [30]. With the unfolding in time of the computation involved in the forward computation, RNN will generate very deep feed forward networks to learn long-term dependencies, which is an intractable task for ordinary RNN [31]. Therefore, several specialized memory units have been developed—for example, the long short term memory cell [32] and gated recurrent unit [33]. In this study, in order to make full use of the time series characteristics (TSC) of water quality parameters and avoid the long-term dependence problem of ordinary RNN, the LSTM network model is established to predict the concentration of major pollutants in lakes and the changing trend of lake water quality, so as to provide reference for water quality control and water resources development and utilization [34].

Our main contributions can be summarized as follows:

I) An LSTM network model is proposed to process events with relatively long-time intervals and lags in time series that cannot be achieved by ordinary RNN.

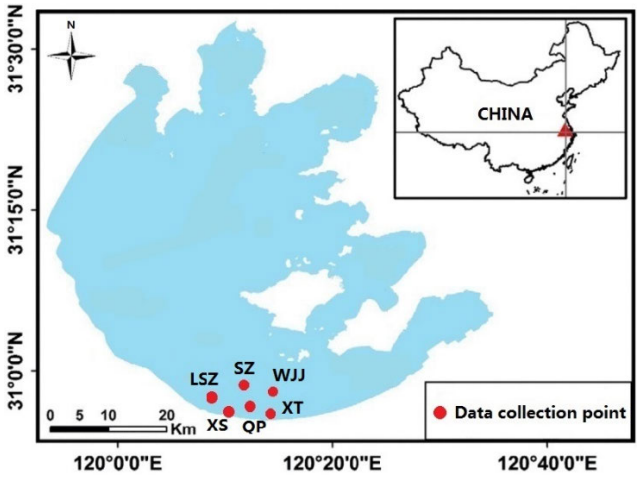

FIGURE 1. Study area.

II) Analyze the variation trends of water quality parameters according to the measured data set, and combine the analysis results with the spectral information of remote sensing images to train the model, which, to some extent, solve the problem that the accuracy of inversion of water quality parameters using only spectral data is not satisfactory.

III) A concrete scheme for monitoring water quality parameters is proposed, which is to train the model using the preprocessed data, and the obtained model is further used to invert the water quality parameters. In addition, the model is applied to satellite images of various periods to obtain the water quality parameter concentration of each pixel, and the water quality changes are continuously monitored in the whole space area and multiple time series.

IV) The pollutant concentration distribution map in the study area is generated, which provides a direction for the subsequent targeted management of water resources.

The rest of the paper is organized as follows: data acquisition and preprocessing are introduced in Section 2. Section 3 describes the basic concept of LSTM network. In Section 4, the LSTM inversion model is depicted. Results and discussion are presented in Section 5. Section 6 narrated conclusion.

II. DATA

A. STUDY AREA

As shown in Figure 1, the overall study area is Taihu Lake in China (the red triangle), which is vast with a surface water area of about 2,338.1 square kilometers. As the third largest freshwater lake in China, Taihu Lake has a water depth of 2 m to 5 m all year round [35]. It plays a vital role in flood storage, water supply, irrigation, navigation and tourism. Therefore, its water quality affects the water safety of thousands of families.

The red dots in Figure 1 represent the data collection points of the six monitoring stations. The six monitoring

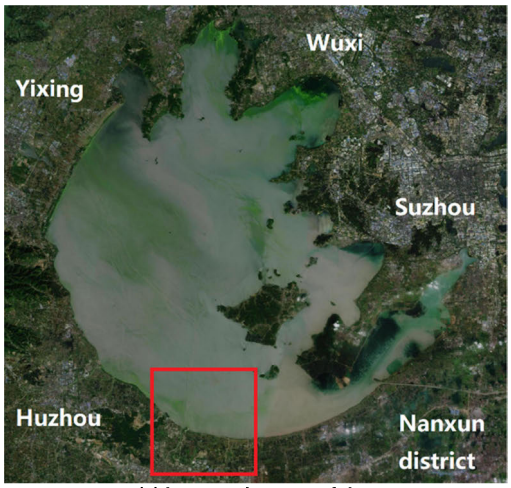

(a) Intercepting part of the water

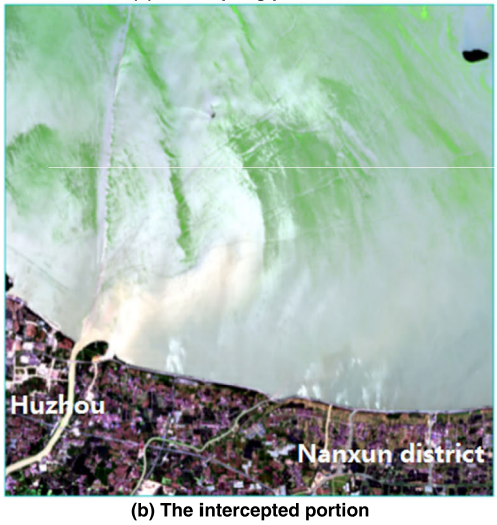

(b) The intercepted portion

FIGURE 2. Interception of the southern waters of Taihu Lake.

stations are Shazhu in Wuxi, Jiangsu province (SZ), Xishan in Suzhou, Jiangsu province (XS), Lanshanzui in Yixing, Jiangsu province (LSZ), Jishui port, Qingpu district, Shanghai (QP), Wangjiangjing in Jiaxing, Zhejiang province (WJJ), and Xintang port in Huzhou, Zhejiang province (XT).

Due to the distribution characteristics of the data collection points, we intercepted a portion containing all these data collection points (the red transparent square of Figure 2(a)). Figure 2(b) is the intercepted result. Moreover, the intercepted area contains both tributaries and dense residential areas, as well as deep water areas. These features make the area have the ability to represent the entire Taihu Lake and also provide a reliable and effective data source for the subsequent inversion image operations.

Figure 2(a) is a satellite image of the area where Taihu Lake is located. It can be seen that the lake borders Suzhou in the east, Yixing in the west, Wuxi in the north, and Huzhou in the south. In Figure 2(b), the main tributary that joins Taihu Lake is called Huanqingxi, followed by three ring canals.

Generally, there are two methods for extracting water areas using remote sensing information: traditional methods based on band spectral values and operations and water body

(a) NDWI (b) MNDWI (c) Mathematical morphology

FIGURE 3. Water extraction.

index methods based on various water-body indexes [36]. The traditional methods are mainly the single-band threshold method and the spectrum-photometric method. The water index method used in this study is a derivative method of the spectrum-photometric method and is the most widely used method to extract water at present, mainly including normalized differential water index method (NDWI) and modified NDWI method (MNDWI) [37]. The basic principle of the water index method is to make use of some specific bands to conduct normalized difference treatment according to the spectral characteristics of the water body, so as to highlight water body region and restrain non-water body region.

In 1996, McFeeters first proposed the NDWI [38], which is defined as (1):

$$NDWI = \frac{p(Green) - p(NIR)}{p(Green) + p(NIR)} \tag{1}$$

where *p(Green)* is the reflectance of the green band, and *p(NIR)* is the reflectance of the near-infrared band.

Using NDWI to extract water is effective, but it has certain limitations. Figure 3(a) is the result of using NDWI to extract the water areas of Figure 2(b), where the white area is the water area and the black area is the non-water area such as urban buildings. It can be found that large water areas are basically extracted, but there are certain misjudgments in areas with many building backgrounds.

On this basis, Xu conducted numerous comparative experiments and proposed the MNDWI [39], which improved the shortcoming of NDWI's large error in the urban architectural background and solved the problem of difficulty in distinguishing water areas from building shadows [40]. Figure 3(b) is the result of using MNDWI to extract the water area of Figure 2(b). The formula of MNDWI is:

$$MNDWI = \frac{p(Green) - p(MIR)}{p(Green) + p(MIR)} \tag{2}$$

where p(MIR) is the reflectance of the mid-infrared band with a wavelength of 770μm to 900μm.

Figure 3(c) is the result of processing Figure 3(b) by mathematical morphology method, which removes the small and disconnected areas, and only retains the shape of the entire lake and the main river.

Figure 3 shows the results of extracting the water areas in Figure 2(b) using different methods. In the process of water extracting, the threshold is set as 0. Values greater than 0 indicate water areas, which are shown as white. Values less than 0 indicate non-water areas, which are shown as black. It can be seen from Figure 3(a) that when the NDWI method is used to extract water, misjudgments occur in both the water and the non-water areas. When the MNDWI method is used to extract water, although the result is better than that of NDWI, there are still many misjudgments in the non-water area (Figure 3(b)). However, these errors were corrected after mathematical morphological processing (Figure 3(c)). Therefore, this study used the MNDWI method to extract the water body and then used mathematical morphology method for further processing.

B. TSC OF WATER QUALITY PARAMETERS

Time series refers to the numerical sequence of the observed values of a statistical index arranged according to the time sequence [41]. The measured values of water quality parameters obtained from water quality monitoring stations are arranged in chronological order, forming a time series [42]. Due to the change of natural environment and human intervention, water quality parameters often fluctuate within a small range in the overall trend of change, but the trend is more obvious in a period. For example, at the turn of spring and summer, the overall DO decreased, while the COD_{Mn} increased. In addition, water quality parameters showed obvious seasonal changes, with higher DO and lower COD_{Mn} due to reduced aquatic biological activities in the winter.

We collected weekly data of each water quality parameter from 2013 to 2015 at the monitoring station XS, and further generated a line chart as shown in Figure 4. Figure 4(a), 4(b), 4(c), and 4(d) respectively show the change trend of PH value and that of the content of DO, COD_{Mn} and NH_3-H during this period. It can be clearly seen that PH, DO and COD_{Mn} all have certain periodicity. However, NH_3-H has no obvious periodicity, the main reason is that there are many external factors that can affect it, which leads to a large fluctuation of its line chart.

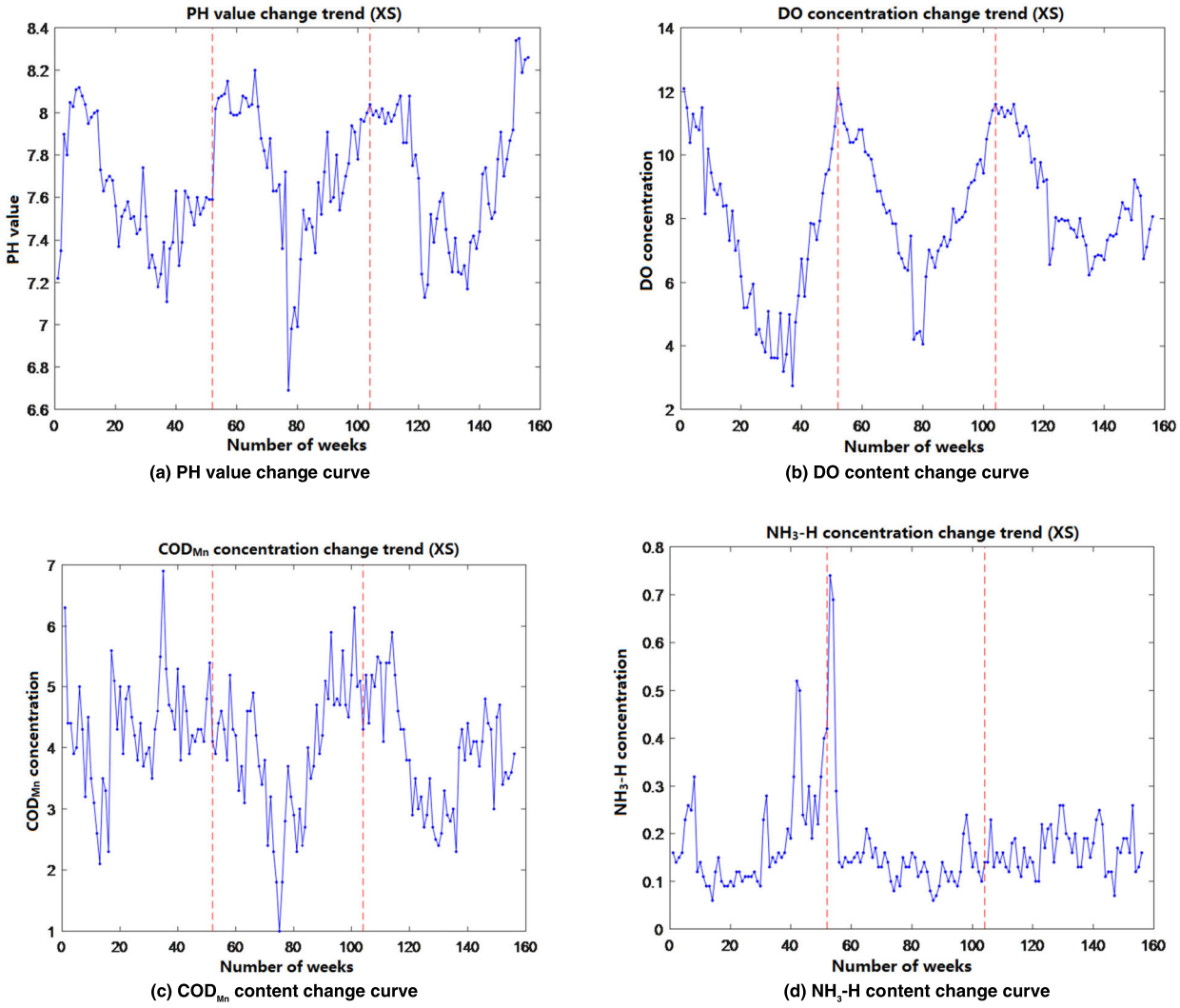

FIGURE 4. Changes trend of 4 water quality parameters.

C. DATA ACQUISITION

Landsat-8 was launched from Vandenberg Air Force Base, California, on February 11, 2013, carrying two sensors: operational land imager (OLI) and thermal infrared sensor (TIRS), and the remote sensing data used in this article comes from the former. Table 1 shows the parameters and main uses of each band of OLI.

The open-use Landsat-8 data is divided into four levels. Among them, the L0Rp data is a lower level, which is only processed by framing and cataloging, and generally used for radiation correction and geometric correction. The L1G data is the data after the preliminary geometric correction, but it lacks the matching with the digital elevation model. L1Gt level data is obtained by geometric correction of the system using ground control points and digital elevation model (DEM) data. The L1T data product selected in this article has been subjected to system radiation correction and ground control point geometric correction, and topographic correction has been carried out through DEM.

In the process of constructing the water quality parameter inversion model, each pixel of the satellite image reflects the spectral reflectance of a certain range, while the measured data is the precise value of a certain point. In order to establish

TABLE 1. Band Description of OLI.

No.	Band (μm)	Spatial resolution (m)	main application
1	0.433-0.453	30	Coastal zone observation
2	0.450-0.515	30	Water penetration, vegetation discrimination
3	0.525-0.600	30	Distinguish between vegetation
4	0.630-0.680	30	Identify roads, bare soil and vegetation types
5	0.845-0.885	30	Soil identification and biomass estimation
6	1.560-1.660	30	Identify roads, exposed soil and clouds
7	2.100-2.300	30	Identify minerals, vegetation and soil
8	0.500-0.680	15	Enhanced resolution
9	1.360-1.390	30	cloud detection

TABLE 2. The Indicators Used to Evaluate the Model.

Index	Computational formula	Meaning
R^2	$R^2 = 1 - \left[\sum_{i=1}^{n}\left(y_i - y_i\right)^2 / \sum_{i=1}^{n}\left(y_i - \overline{y_i}\right)^2\right]$	The degree to which the predicted value fits the true data.
RMSE	$RMSE = \sqrt{\sum_{i=1}^{n}\left(y_i - y_i\right)^2 / n}$	The difference between the inversion value and the true value.
rRMSE	$rRMSE = RMSE - \overline{y}$	The amount of deviation between the inversion value and the true data.
MRE	$MRE = \left[\sum_{i=1}^{n}\left\lvert\left(y_i - y_i\right) / y_i\right\rvert\right] / n$	The average deviation of the error from the true value.
E_{max}	$E_{max} = \left\lvert\max\left(y_i - y_i\right)\right\rvert$	The maximum range of error between inversion value and true value.
E_{min}	$E_{min} = \left\lvert\min\left(y_i - y_i\right)\right\rvert$	The minimum error between the inversion value and the true value.

the correspondence between them, it is necessary to match the two kinds of data [43]. We obtained the measured weekly data of four water quality parameters and water quality evaluation grade from 2013 to 2018 from six monitoring stations in Taihu Lake. After removing some invalid data caused by the satellite return visit cycle and cloud cover, these water quality parameters are matched with the spectral data of each band of remote sensing images on date and geographical coordinates. The matched data is used to train the model.

D. PERFORMANCE METRICS

It is necessary to evaluate the performance of a model before practical application. The evaluation of the inversion model includes evaluation of its accuracy, stability and model prediction ability, and the result is determined by R^2, root-mean-square error (RMSE), rRMSE, MRE, maximum absolute error (E_{max}), and minimum absolute error (E_{min}). The detailed description is shown in Table 2.

In Table 2, y_i is the measured value of the *ith* sample, $\widehat{y_i}$ is the inversion value of the *ith* sample, $\overline{y_i}$ is the average value of the sample, and n is the total number of the sample.

III. BASIC CONCEPTS OF LSTM NETWORK

A. RNN

The change trend of the water quality parameters analyzed in this article are not completely random. They are not only related to the spectral curve of remote sensing images, but also closely related to the parameter values of the past moments, and their changes have certain gradual characteristics. Figure 4 also shows that the measured sample data has the characteristics of trend, seasonality and periodicity, so the data can be treated as a time series, that is, the current output of the series is determined by the current input and the previous input. In order to use as much historical data of water quality parameters as possible and make full use

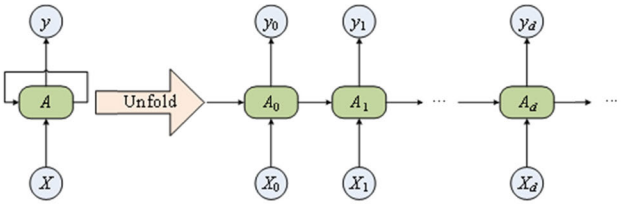

FIGURE 5. Ordinary RNN sequential logic architecture.

of the TSC of water quality parameters, RNN is proposed to process sequence data, which can better predict data with time sequence due to its memory of previous moment information.

Different from traditional neural networks, RNN introduces state variables to store previous information and use them to jointly determine the current output with the current input [44]. This feature makes RNN the most natural neural network structure for dealing with time-series related problems, and it is widely used in speech recognition, language modeling, machine translation and timing analysis. The temporal logic architecture of an ordinary RNN is shown in Figure 5.

As shown in Figure 5, RNN has an input X_d at each moment, and then determines an output y_d together with the current state A_d. A_d is calculated from the state A_{d-1} at the previous moment and the current input X_d (refer to (3)). Equation (4) is the calculation formula of the output layer. A_i retains the crucial features of the information at the current moment and the previous moment, and then predicts what will happen next with a high probability based on these characteristics. Note that RNN requires an input at every moment, but not an output at every moment. Moreover, parameters in the network are shared at different times.

$$A_d = f\left(U \times X_d + W \times A_{d-1}\right) \tag{3}$$

where f is the activation function. U and W are input weight matrix and memory weight matrix respectively.

$$y_i = soft\max\left(V \times A_i\right) \tag{4}$$

where *softmax* is the classifier, V is the output weight matrix, and y_i is the output with high probability.

Although it is proposed to process sequence information, ordinary RNN do not perform well when dealing with longer sequences. This is due to the back propagation method used in deep neural network training. In the process of calculating the gradient of each layer, the multiplication operations will be involved. When the factor of continuous multiplication is less than 1, once the network is too deep, the gradient update information obtained will decay exponentially, and then the vanishing gradient problem will occur. On the other hand, if the factor of continuous multiplication is greater than 1, as the network deepens, the gradient update information finally obtained will increase exponentially, and then the exploding gradient problem will occur.

Although RNN can theoretically establish the dependence relationship between long-term intervals states, it is difficult for RNN to establish such a long-distance dependence relationship due to the problem of vanishing gradient or

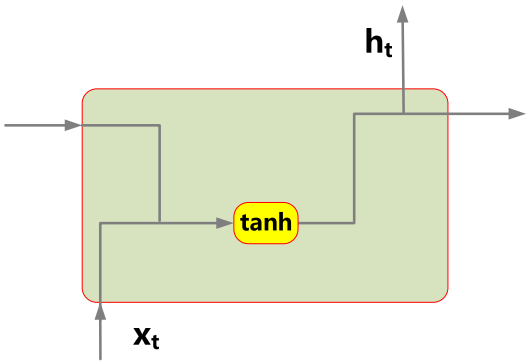

FIGURE 6. The logical structure of a hidden unit in ordinary RNN.

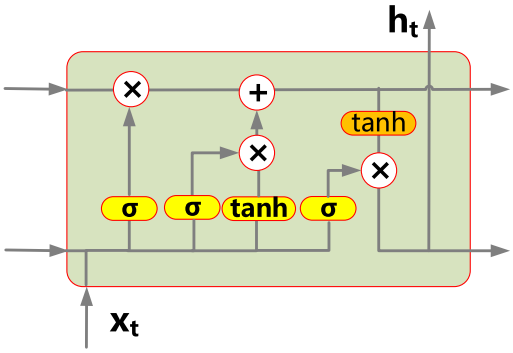

FIGURE 7. The logical structure of a hidden unit in LSTM network.

exploding gradient. The problem with the exploding gradient is usually solved by adding a threshold in the network: when the gradient exceeds the threshold, the network intercepts the data directly, thus suppressing the gradient explosion. However, there is no solution for the vanishing gradient problem for a long time, which makes it difficult for RNN to capture the dependence of the large time step distance in the time series in practice. Therefore, the deep learning technique known as LSTM network is proposed to resolve the vanishing gradient problem [45].

B. LSTM

LSTM is a deformed structure of RNN, which overcomes the problem of vanishing gradient and achieves controllable memory information on time series by adding memory units in each neuron in the hidden layer of ordinary RNN. Each unit of the hidden layer uses several controllable gates (forget gate (FG), input gate (IG), candidate gate (CG), and output gate (OG)) to determine which of the previous and current information is removed or retained, thereby achieving long-term memory of the RNN network. The structure of each gate is very simple and consists of a sigmoid function (σ) and a point multiplication operation.

The improvement of RNN by LSTM can be seen more intuitively through the two pictures below. Figure 6 is a logical structure diagram of a hidden unit of an ordinary RNN, and Figure 7 is a logical structure diagram of an LSTM hidden unit. It can be seen that the difference between LSTM and ordinary RNN is that its hidden layer unit is no longer just an activation function, but the previous and current information are screened together by FG, IG, CG and OG. Such a network structure solves the exploding gradient while avoiding the vanishing gradient, and realizes the long-term memory function of the sequential data.

The key to LSTM's long-term memory is the control of the cell state. The cell's state is transmitted from left to right along this line (The black solid line in Figure 8), and only a few simple linear operations are carried out in this process, so that the information will basically not change during the transmission process (Figure8). And this means of managing cell state by linear manipulation of neurons is called gate operation. c_{t-1} represents the cell state at the previous moment, and c_t represents the current cell state.

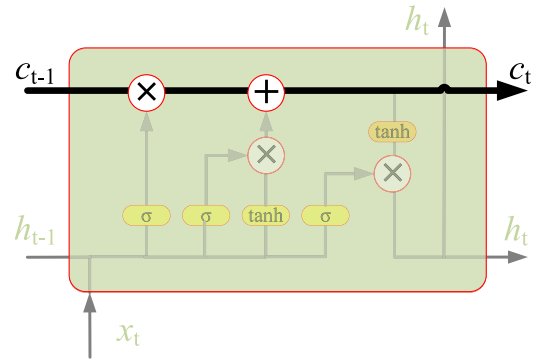

FIGURE 8. Schematic diagram of cell state transfer.

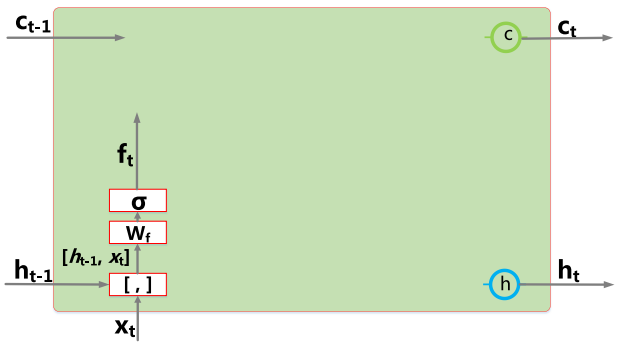

FIGURE 9. The logical structure of FG.

The simplest LSTM network uses FG, IG, and OG to control the cell state. Nonetheless, in order to facilitate the presentation, a CG is generally added to control the proportion of the information at previous moment and the input information at current moment. By using controllable gate to accurately select forgetting, storing and transferring information, LSTM solves the long-term dependence problem of ordinary RNN. The following describes the concrete operation process of these four gates.

1) As shown in Figure 9, FG decides what and how much information is forgotten in c_{t-1}. f_t is the output of FG at tth time (refer to (5)).

$$f_t = \sigma\left(W_f \bullet [h_{t-1}, x_i] + b_f\right) \tag{5}$$

where W_f is the weight matrix of the FG; b_f is the bias of FG; $[h_{t-1}, x_t]$ means connect h_{t-1} and x_t into a vector.

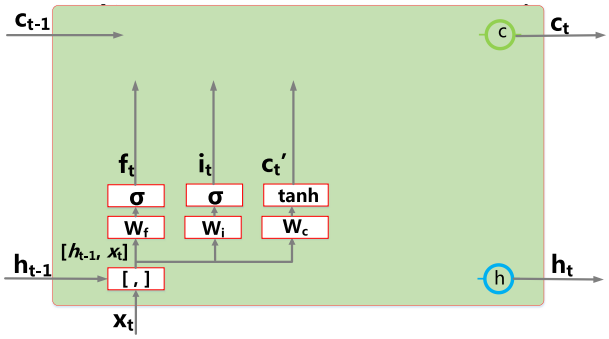

FIGURE 10. The logical structure of information input.

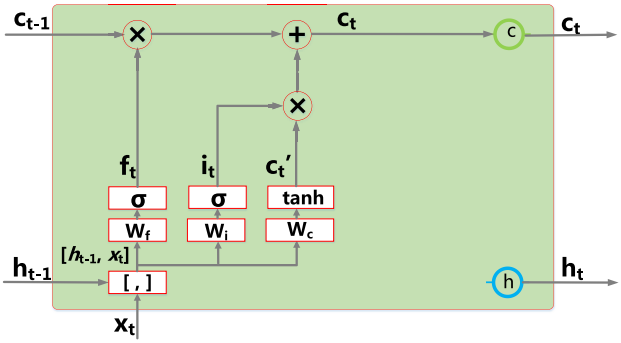

FIGURE 11. The logical structure that updates the cell state.

2) As shown in Figure 10, IG determines which new information can be added to c_t (refer to (6)). In addition, a new candidate c_t' is generated using the tanh function in CG and a value between -1 and 1 is obtained (refer to (7)). c_t' retains new cell state information that may need to be transmitted.

$$i_t = \sigma\left(W_i \bullet [h_{t-1}, x_t] + b_i\right) \tag{6}$$

$$c_t' = \tanh\left(W_c \bullet [h_{t-1}, x_t] + b_c\right) \tag{7}$$

where W_i and W_c are the weight matrix of IG and CG respectively, b_i and b_c are the bias of IG and CG respectively.

3) As shown in Figure 11, the part of the cell state that need to be preserved obtained after FG screening are integrated with c_t' to obtain c_t (refer to (8)). If the output value of FG is 1 or approximately 1 while the output of IG is 0 or approximately 0, the cell state information will not change, and it will be directly passed to the next hidden unit, that is, $c_t = c_{t-1}$.

$$c_t = f_t \times c_{t-1} + i_t \times c_t' \tag{8}$$

4) OG determines what kind of information can be output. As shown in Figure 12, first, use the sigmoid function to select what kind of information to output (refer to (9)); then c_t is obtained by the tanh function as a vector in the range $(-1, 1)$; eventually, the two parts are multiplied and then the result is output (refer to (10)). The state of the hidden layer output by OG (i.e. h_t) is composed of input information and cell state. Moreover, when the output of the sigmoid function is 1 or approximately 1, c_t will participate in the calculation of h_t; otherwise, c_t will be directly output to the next hidden unit.

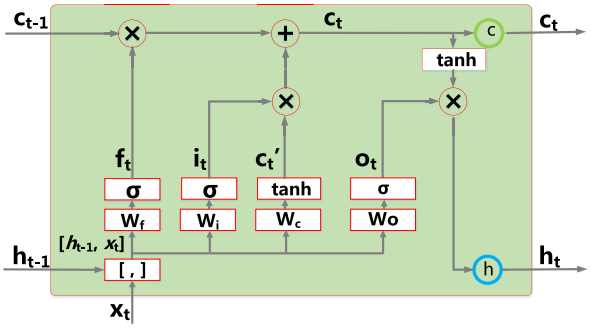

FIGURE 12. A logical structure diagram of information output.

$$o_t = \sigma\left(W_o \bullet [h_{t-1}, x_t] + b_o\right) \tag{9}$$

$$h_t = o_t \times \tanh \tag{10}$$

where W_o is the weight matrix of OG, and b_o is the bias of the OG, and h_t is the state of hidden layer at current moment.

Equations (5) to (10) are all steps of LSTM forward calculation. The complete logical structure is shown in Figure 12, in which h_{t-1} represents the state of hidden layer at previous moment and x_t represents the input at the current moment. The output interval of the sigmoid function is [0, 1], and the size of the output value of this function determines how much information is transmitted: the smaller the output value, the less information is transmitted.

IV. ESTABLISH AN LSTM NETWORK INVERSION MODEL

Theoretically, when there are two hidden layers in the network, the arbitrary nonlinear mapping relationship between input and output can be constructed. Blindly increasing the number of hidden layers will aggravate the over-fitting risk of the model, and the applicability of the model will be greatly compromised. In this study, an LSTM network model with two hidden layers is established to retrieve the water quality parameters of Taihu Lake. Taking the inversion model of DO content (mg/L) as an example, we set a total of 7 nodes in the input layer, which are spectral reflectance of 6 bands and DO value in the same water at the previous week respectively (Table 3). The node number of the output layer is set to 1, and the inverted value of DO(t) is output.

In this article, the number of hidden layer nodes of the LSTM network is determined according to (11) and the stepwise test method.

$$s = \sqrt{m+n} + \alpha \tag{11}$$

where m and n are the number of nodes in the input layer and the output layer, respectively, α representing the fluctuation range, and constants between 1 and 10 are generally selected.

Before debugging the LSTM model, the learning rate is set to 0.01, and the trial range of the number of hidden layer nodes is set to [4], [15]. The training errors of models under the condition of different number of hidden layer nodes are calculated successively, and the results are shown in Table 4.

TABLE 3. Input Layer Data of LSTM Network Model for DO Inversion.

No.	Input layer data	Explanation
1	Band_1	Spectral reflectance in the 0.433~0.453μm band of this water at this moment
2	Band_2	Spectral reflectance in the0.450~0.515μm band of this water at this moment
3	Band_3	Spectral reflectance in the0.525~0.600μm band of this water at this moment
4	Band_4	Spectral reflectance in the0.630~0.680μm band of this water at this moment
5	Band_5	Spectral reflectance in the0.845~0.885μm band of this water at this moment
6	Band_7	Spectral reflectance in the2.100~2.300μm band of this water at this moment
7	DO(t-1)	The DO value of the water area in the previous week

TABLE 4. The Training Error of the Number of Nodes in Each Model's Hidden Layer.

S	Loss			
	PH	DO	COD_{Mn}	NH_3-H
4	0.009821	0.008691	0.009133	0.009114
5	0.011214	0.010713	0.012513	0.011289
6	**0.007989**	0.010343	0.013369	0.008793
7	0.011408	0.006187	0.011084	0.007680
8	0.015697	**0.005628**	0.014691	0.005621
9	0.014767	0.008212	0.012885	**0.004743**
10	0.010394	0.008188	0.009257	0.009826
11	0.016827	0.007426	0.011403	0.005738
12	0.011395	0.007507	0.006505	0.005623
13	0.015958	0.006889	**0.004300**	0.005247
14	0.015097	0.008868	0.006914	0.006915
15	0.014652	0.007405	0.007702	0.004821

In this table, *S* represents the number of hidden layer nodes, and *Loss* represents the model training error.

It can be seen from Table 4 that the optimal hidden layer nodes of PH, DO, COD_{Mn} and NH_3-H inversion models are 6, 8, 13 and 9, respectively, and the Loss value of each model is the smallest under this condition.

This article uses FLAASH module of ENVI to perform atmospheric correction on satellite images, builds an LSTM network model based on the Python 3.7 platform, with batch_size set to 1. The number of input layer nodes is set to 7, and the number of output layer nodes is 1. The number of hidden layer is set to 2, and the number of nodes varies with the water quality parameters that need to be inverted: the optimal number of PH, DO, COD_{Mn} and NH_3-H are 6, 8, 13, 9 respectively. The training data is the matched spectrum data of each water quality parameter, and the verification data is the measured data.

The algorithm for training the LSTM network is roughly the same as that of the BP network. The difference is that the data processed by the LSTM are time-sequential, which indicates that the error of the entire time point must be back-propagated during the training process. The training method applicable to LSTM is the back-propagation through time algorithm (BPTT). The main steps are:

I) Determine the initial value of each parameter. When the data is transmitted along the input layer to the output layer, the output value of each neuron is calculated in turn, and the value of the loss function is obtained at the same time.
II) The error is transmitted backwards on the two levels of space and time. At the spatial level, the error is transmitted to the upper layer of the network structure; at the time level, the error at the current moment is transmitted to the previous moment is calculated.
III) Calculate the gradient of each weight of each layer.
IV) Repeat I) to III), constantly update the weight to obtain the expected model.

V. RESULTS AND ANALYSIS

A. LSTM NETWORK INVERSION RESULTS

Figure 13 is the comparison between the inversion values of PH, DO, COD_{Mn} and NH_3-H obtained by using the LSTM network and the measured values. Table 5 is the evaluation results of the inversion model by using various evaluation indexes.

Combined with Figure 13 and Table 5, we can find that although there is a slight difference between some inversion values and measured values, the number of samples and the range of the difference are small (Figure 13). The main reason for this gap may be the lack of training data, leading to the inaccuracy of the models. Although the R^2 of the PH inversion model is relatively low among the inversion models of the four parameters, there is not much difference between the inversion value and the measured value (RMSE = 0.4925, rRMSE = 0.0674, MRE = 0.0517, E_{max} = 0.7787, E_{min} = 0), which demonstrates that the possibility of mis-judgment of acid-base or acid-base strength based on the inversion results is very small. Moreover, the R^2 of the DO inversion model is higher than the PH value, but its RMSE is the largest among the four models, and its MRE is also larger, indicating that the model is not robust enough and there are more extreme values with a large distance from the measured value. This may be due to the limitations of the current use of satellite measurements of DO, resulting in a low reliability of the training data on DO. The R^2 of NH_3-H inversion model is the highest among the four models, and the RMSE is small, which means that the inversion value of this model has a high degree of fitting with the measured value, and the model is relatively robust. However, the MRE of this model is the largest, which can be seen from Figure 13(d). Most of the inversion values are distributed around the measured value with a certain distance from these values, making the percentage of the absolute error in the true value higher. The reason for this situation may be that there are many external factors that can affect NH_3-H in water, leading to its poor TSC and affecting the operation of the model. As can be seen from Table 5, after excluding the interference of extreme values, the COD_{Mn} inversion model has the best performance, followed by the PH inversion model. Nonetheless, this method has certain limitations: for example, some water quality parameters are easily affected by external factors, the lack of training data, changes of climatic conditions and applied water area will affect the accuracy of the model.

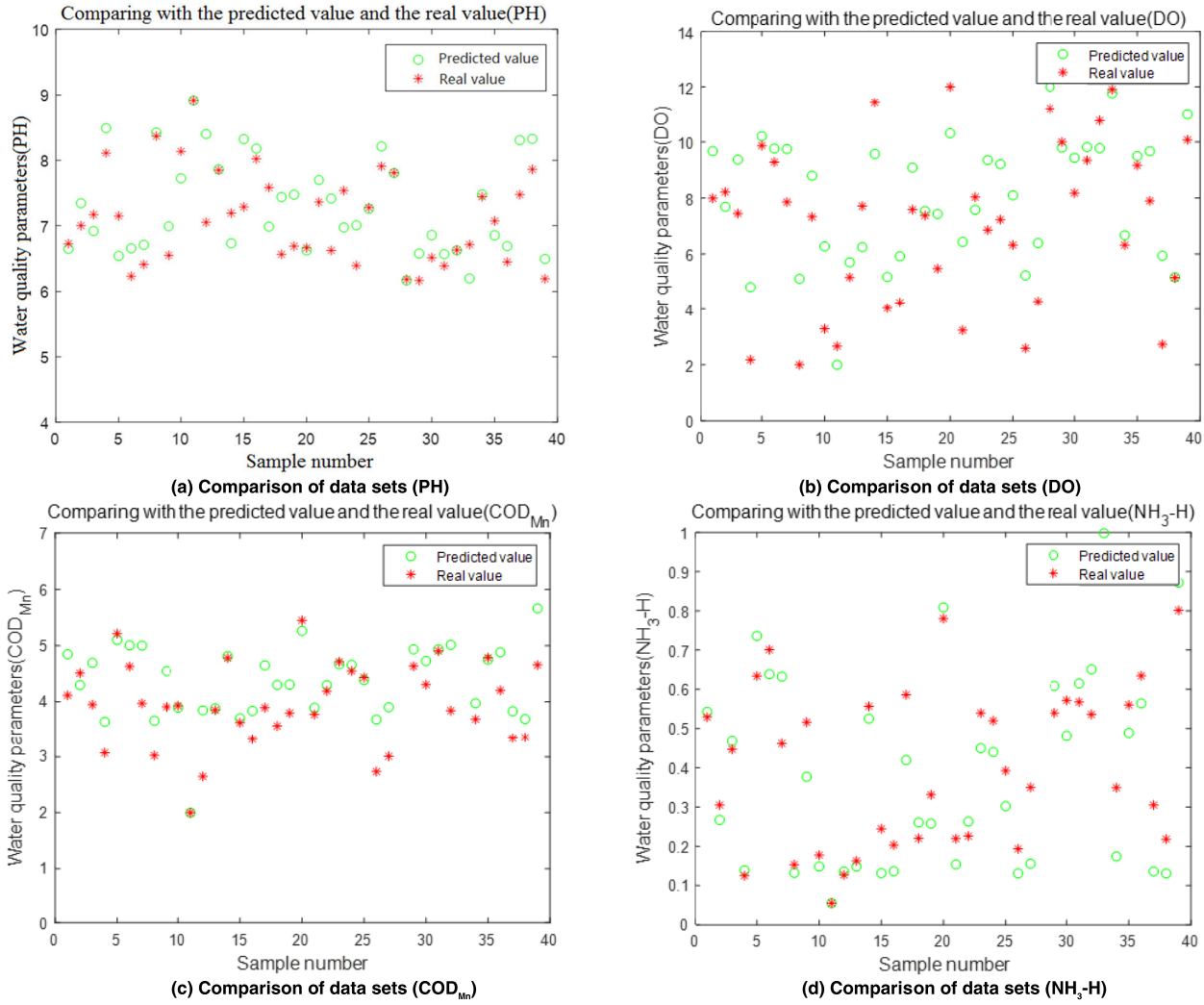

FIGURE 13. Comparison of inversion data and measured data.

TABLE 5. Model Evaluation Results.

Name	R^2	RMSE	rRMSE	MRE	E_{max}	E_{min}
PH	0.7244	0.4925	0.0674	0.0517	0.7787	0
DO	0.8455	1.6856	0.2099	0.2017	1.7054	0
COD_{Mn}	0.8497	0.5531	0.1241	0.0955	1.6612	0.0044
NH_3-H	0.8868	0.0927	0.2519	0.3835	0.2165	0

Applying the model to satellite remote sensing images of various periods, the inverted images of various water quality parameters obtained are shown in Figure 14. Figure 14(a), (b), (c) and (d) are the inverted images of PH, DO, COD_{Mn}, and NH_3-H respectively.

As can be seen from Figure 14(a), the PH in the northern waters is between 8.0 and 9.0, and that in the southeast waters is between 7.0 and 8.0, meeting the requirements of human society for production and life. It should be noted that the southwest waters with a pH value of 6.0 to 7.0 which have a pH lower than the minimum standard of 7.5, are acidic waters. The reason may be that the nearby river carries acidic substances and flows into Taihu Lake; or it may be caused by a nearby factory discharging pollutants into the lake. Attention should be paid to the pollution of the southwestern waters, and the sources of pollution should be treated as soon as possible.

In Figure 14(b), the DO value in the southwest waters is 8.0 to 9.0, and the other parts are 7.0 to 8.0, all of which meet the above evaluation criteria of not less than 4. This indicates that the water area contains more oxygen, which also reflects its higher self-purification ability from the side. The reason for the difference in DO value in this water area may be the difference between the depth of the near shore and the center of the lake: the deeper the water layer, the lower the DO content; besides, when the algae in the water increase, oxygen released by photosynthesis makes the water DO very high.

The water area in Figure 14(c) can be roughly divided into three parts according to COD_{Mn}concentration. The first part is the dark gray area in the north, COD_{Mn} is 3 to 4; the second part is the light gray area in the southeast, and the COD_{Mn} is 4 to 5; the third part is the white area in the southwest,

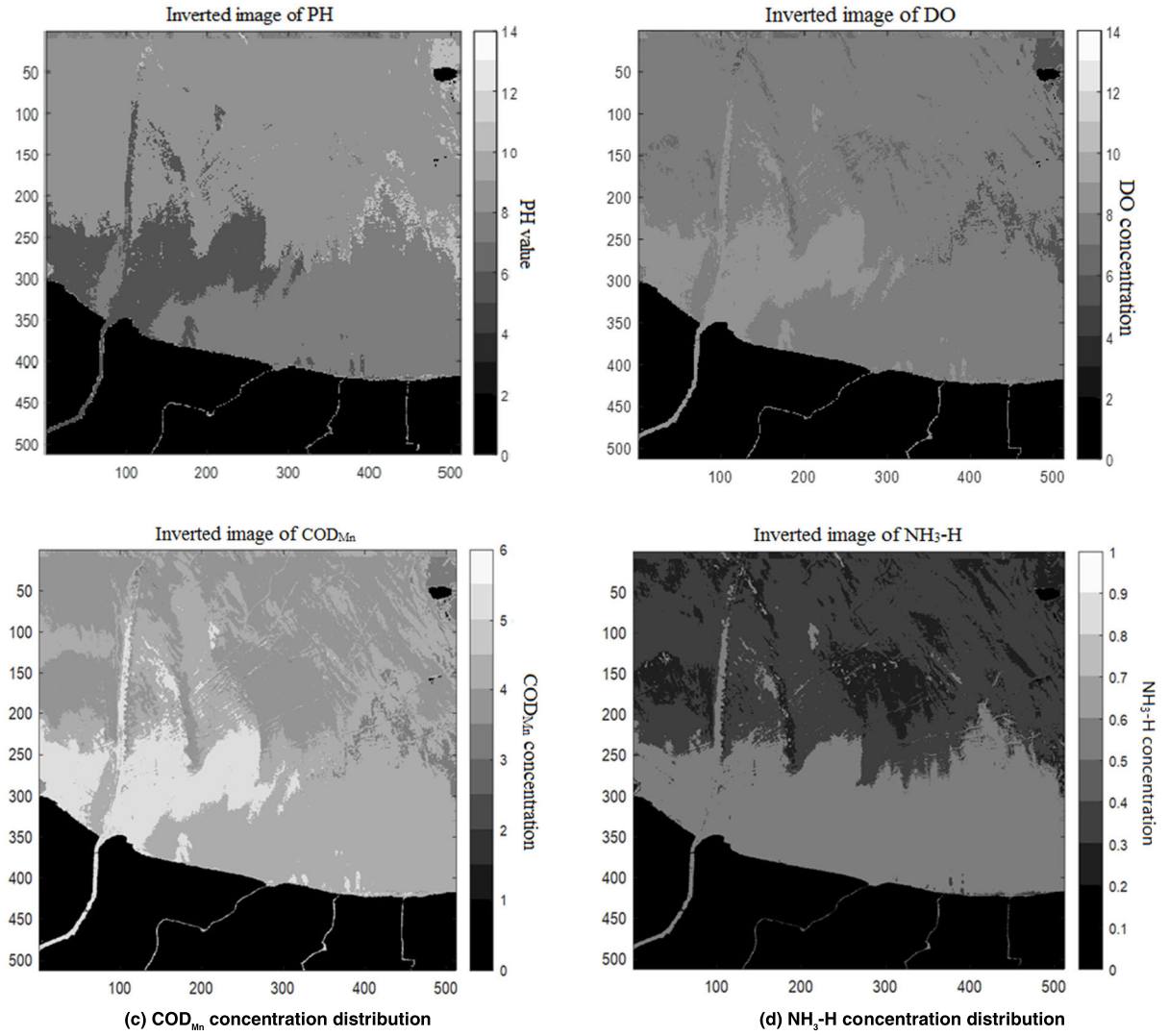

FIGURE 14. Inverted images.

and the COD_{Mn} is 5.5 to 6.0. The higher the COD_{Mn} in water, the more serious the pollution by organic matter. The sources of these organic matter pollution may be pesticides, chemical plants, organic fertilizers, etc. If left untreated, many organic pollutants may be deposited on the bottom of the lake, causing lasting poisoning to aquatic organisms for several years.

In Figure 14(d), the concentration of NH_3-H in the northern waters is 0.2 to 0.4, while that in the southern waters is 0.5 to 0.7, which is corresponding to the PH distribution in Figure 14(a). Corresponding to the distribution of PH, the NH_3-H content is high in the waters with high PH in the north, and the NH_3-H content is low in the waters with relatively low PH in the south. The reason why the NH_3-H content in the northern waters is too high may be partly because the temperature rise causes the PH of the water to increase, which in turn affects the NH_3-H content; the other part may be that domestic sewage or industrial sewage is discharged here, causing the rise of NH_3-H. Regardless of the cause, the increased NH_3-H concentration in the water can poison aquatic organisms and threaten human health.

In summary, the coastal areas of Taihu Lake, especially the waters with tributaries, have low PH, and are seriously polluted by organic materials. Therefore, it is necessary to take measures as soon as possible to control the spread of the polluted waters along the Taihu Lake.

B. COMPARE EXPERIMENTAL RESULTS

In order to reflect the advantages of the proposed model, we implemented comparative experiment, including two traditional empirical methods: single band linear regression (SR) and multiband linear regression (MR), as well as BP neural network (BP), to monitor the four water quality parameters and evaluate the results. The evaluation results are shown in Figure 15.

In SR, the spectral bands in Table 3 that have the best correlation with each water quality parameter are selected to establish empirical formulas: Band_5, Band_7, Band_5 and Band_4 are associated with PH, DO, COD_{Mn}, and NH_3-H, respectively. In MR, the empirical of each water quality parameter is established by combining multiple spectral

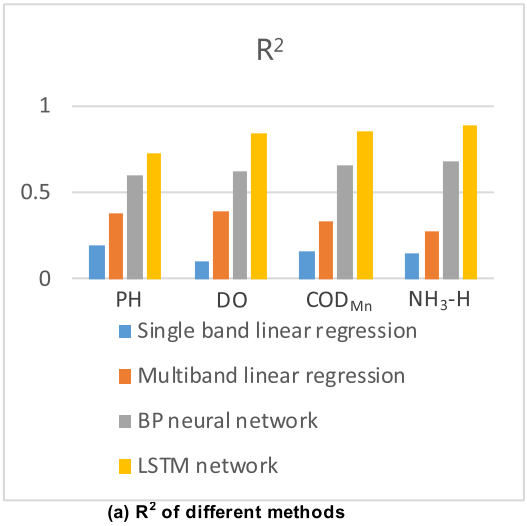

(a) R^2 of different methods

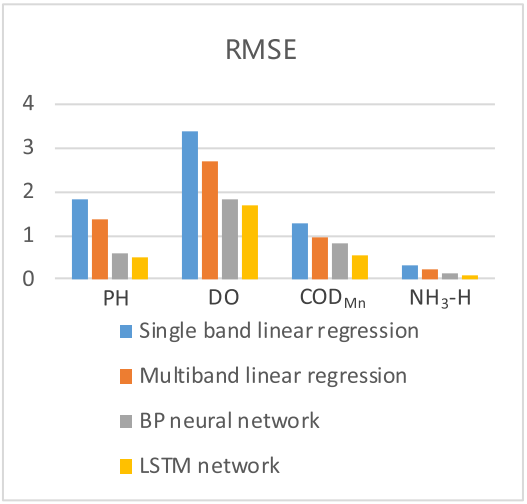

(b) RMSE of different methods

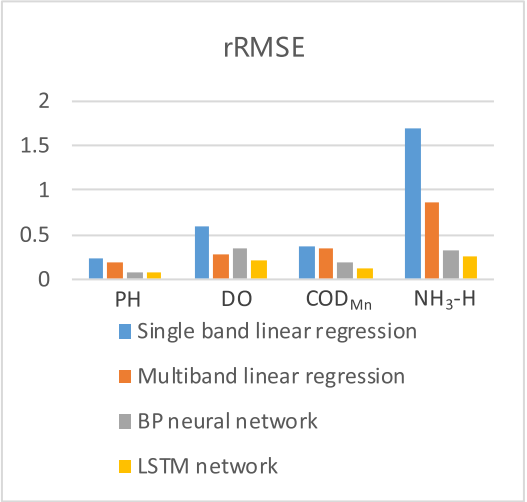

(c) rRMSE of different methods

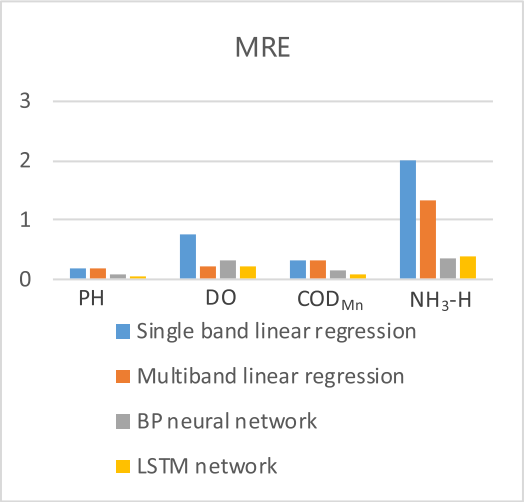

(d) MRE of different methods

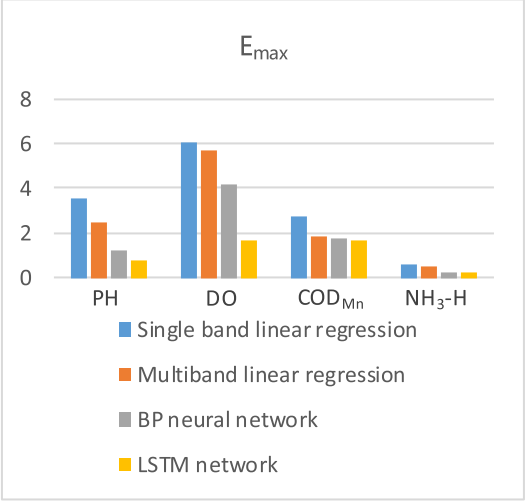

(e) E_{max} of different methods

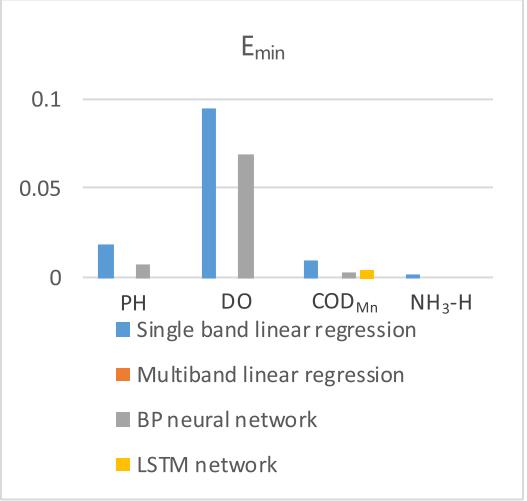

(f) E_{min} of different methods

FIGURE 15. Evaluation results of different methods.

bands. In BP, the parameter setting is consistent with that of LSTM.

It can be seen from the figure that among the four methods, the performance of the neural network methods is better than that of the traditional methods in various evaluation indicators, and the performance of LSTM is better than that of BP. Although in Figure 15(d), in the experiment of inverting NH_3-H, the MRE of LSTM is higher than that of BP,

the difference is only 3.24%, which does not affect the overall evaluation result, that is, the performance of LSTM is the most satisfactory.

VI. CONCLUSION

Long-term dynamic monitoring of water quality has critical and far-reaching significant for human social life, industrial production and agricultural irrigation. In the research of water quality monitoring, the combination of satellite remote sensing images and machine learning has become a focus of attention. In order to retain as much historical data as possible and accurately predict future changes in water quality, this article establishes an inversion model based on LSTM network to conduct inversion for four important parameters for water quality assessment, including PH, DO, COD_{Mn} and NH_3-H. Experimental results show that the accuracy of the four models is satisfactory: the R^2 of the model is around 0.83, the rRMSE is around 0.16, and the MRE is around 0.18. Moreover, the LSTM network model is applied to the images of each period to obtain the water quality parameter concentration of each pixel, and the corresponding inversion image is further generated. The generated inversion images are basically consistent with official information. It is realized to monitor the water quality change of Taihu Lake continuously with whole space region and multi-time series. Comparative experiments with other methods also show the advantages of the proposed model. Experimental results on Taihu Lake show that, when there is a clear and coherent historical data in the same water area, the LSTM network model is chosen to retrieve water quality parameters and the results are highly accurate, the model is robust and performs well, and has the ability to meet the basic requirements of actual water quality monitoring.

REFERENCES

[1] C. J. Vörösmarty, P. B. McIntyre, M. O. Gessner, D. Dudgeon, A. Prusevich, P. Green, S. Glidden, S. E. Bunn, C. A. Sullivan, C. R. Liermann, and P. M. Davies, "Global threats to human water security and river biodiversity," *Nature*, vol. 467, no. 7315, pp. 555–561, Sep. 2010.

[2] C. Doña, J. M. Sánchez, V. Caselles, J. A. Domínguez, and A. Camacho, "Empirical relationships for monitoring water quality of lakes and reservoirs through multispectral images," *IEEE J. Sel. Topics Appl. Earth Observ. Remote Sens.*, vol. 7, no. 5, pp. 1632–1641, May 2014, doi: 10.1109/JSTARS.2014.2301295.

[3] Y. Sun, Z. Chen, G. Wu, Q. Wu, F. Zhang, Z. Niu, and H.-Y. Hu, "Characteristics of water quality of municipal wastewater treatment plants in China: Implications for resources utilization and management," *J. Cleaner Prod.*, vol. 131, pp. 1–9, Sep. 2016.

[4] W. A. C. Udeshani, H. M. K. P. Dissanayake, S. K. Gunatilake, and R. Chandrajith, "Assessment of groundwater quality using water quality index (WQI): A case study of a hard rock terrain in Sri Lanka," *Groundwater Sustain. Develop.*, vol. 11, no. 2352-801X, Oct. 2020, Art. no. 100421.

[5] N. Benouara, A. Laraba, and L. Hachemi Rachedi, "Assessment of groundwater quality in the seraidi region (north-east of Algeria) using NSF-WQI," *Water Supply*, vol. 16, no. 4, pp. 1132–1137, Aug. 2016.

[6] M. Saberioon, J. Brom, V. Nedbal, P. Souček, and P. Císař, "Chlorophyll—A and total suspended solids retrieval and mapping using sentinel-2A and machine learning for inland waters," *Ecological Indicators*, vol. 113, Jun. 2020, Art. no. 106236.

[7] C. G. Griffin, J. W. McClelland, K. E. Frey, G. Fiske, and R. M. Holmes, "Quantifying CDOM and DOC in major arctic rivers during ice-free conditions using landsat TM and ETM+ data," *Remote Sens. Environ.*, vol. 209, pp. 395–409, May 2018.

[8] J. Chen, W.-N. Zhu, Y. Q. Tian, and Q. Yu, "Estimation of colored dissolved organic matter from Landsat-8 imagery for complex inland water: Case study of lake huron," *IEEE Trans. Geosci. Remote Sens.*, vol. 55, no. 4, pp. 2201–2212, Apr. 2017, doi: 10.1109/TGRS.2016.2638828.

[9] J. Xia, G. Xu, P. Guo, H. Peng, X. Zhang, Y. Wang, and W. Zhang, "Tempo-spatial analysis of water quality in the three gorges reservoir, China, after its 175-m experimental impoundment," *Water Resour. Manage.*, vol. 32, no. 9, pp. 2937–2954, Jul. 2018.

[10] E. Avigliano and N. Schenone, "Water quality in Atlantic rainforest mountain rivers (South America): Quality indices assessment, nutrients distribution, and consumption effect," *Environ. Sci. Pollut. Res.*, vol. 23, no. 15, pp. 15063–15075, Aug. 2016.

[11] M. Dunbabin and L. Marques, "Robots for environmental monitoring: Signifificant advancements and applications," *IEEE Robot. Autom. Mag.*, vol. 19, no. 1, pp. 24–39, Mar. 2012.

[12] Y. Qiao, J. Feng, X. Liu, W. Wang, P. Zhang, and L. Zhu, "Surface water pH variations and trends in China from 2004 to 2014," *Environ. Monitor. Assessment*, vol. 188, no. 7, p. 443, Jul. 2016.

[13] A. Csábrági, S. Molnár, P. Tanos, J. Kovács, M. Molnár, I. Szabó, and I. G. Hatvani, "Estimation of dissolved oxygen in riverine ecosystems: Comparison of differently optimized neural networks," *Ecological Eng.*, vol. 138, pp. 298–309, Nov. 2019.

[14] K. Singh, P. Kumar, and B. K. Singh, "An associative relational impact of water quality on crop yield: A comprehensive index analysis using LISS-III sensor," *IEEE Sensors J.*, vol. 13, no. 12, pp. 4912–4917, Dec. 2013, doi: 10.1109/JSEN.2013.2276760.

[15] G. Cazaudehore, B. Schraauwers, C. Peyrelasse, C. Lagnet, and F. Monlau, "Determination of chemical oxygen demand of agricultural wastes by combining acid hydrolysis and commercial COD kit analysis," *J. Environ. Manage.*, vol. 250, Nov. 2019, Art. no. 109464.

[16] M. C. Vogt and M. E. Vogt, "Research article: Near-remote sensing of water turbidity using small unmanned aircraft systems," *Environ. Pract.*, vol. 18, no. 1, pp. 18–31, Mar. 2016.

[17] B. Arabi, M. S. Salama, J. Pitarch, and W. Verhoef, "Integration of *in-situ* and multi-sensor satellite observations for long-term water quality monitoring in coastal areas," *Remote Sens. Environ.*, vol. 239, Mar. 2020, Art. no. 111632.

[18] F. Gohin, D. Van der Zande, G. Tilstone, M. A. Eleveld, A. Lefebvre, F. Andrieux-Loyer, A. N. Blauw, P. Bryère, D. Devreker, P. Garnesson, T. H. Fariñas, Y. Lamaury, L. Lampert, H. Lavigne, F. Menet-Nedelec, S. Pardo, and B. Saulquin, "Twenty years of satellite and *in situ* observations of surface chlorophyll—A from the northern bay of Biscay to the eastern English channel. Is the water quality improving?" *Remote Sens. Environ.*, vol. 233, Nov. 2019, Art. no. 111343.

[19] R. T. Ford and A. Vodacek, "Determining improvements in landsat spectral sampling for inland water quality monitoring," *Sci. Remote Sens.*, vol. 1, Jun. 2020, Art. no. 100005.

[20] J. Li, Q. Yu, Y. Q. Tian, B. L. Becker, P. Siqueira, and N. Torbick, "Spatio-temporal variations of CDOM in shallow inland waters from a semi-analytical inversion of Landsat-8," *Remote Sens. Environ.*, vol. 218, pp. 189–200, Dec. 2018.

[21] T. Kutser, B. Paavel, C. Verpoorter, M. Ligi, T. Soomets, K. Toming, and G. Casal, "Remote sensing of black lakes and using 810 nm reflectance peak for retrieving water quality parameters of optically complex waters," *Remote Sens.*, vol. 8, no. 6, p. 497, Jun. 2016.

[22] B. L. Markham, J. C. Storey, D. L. Williams, and J. R. Irons, "Landsat sensor performance: History and current status," *IEEE Trans. Geosci. Remote Sens.*, vol. 42, no. 12, pp. 2691–2694, Dec. 2004, doi: 10.1109/TGRS.2004.840720.

[23] K. Peterson, V. Sagan, P. Sidike, A. Cox, and M. Martinez, "Suspended sediment concentration estimation from landsat imagery along the lower Missouri and middle Mississippi rivers using an extreme learning machine," *Remote Sens.*, vol. 10, no. 10, p. 1503, Sep. 2018.

[24] K. T. Peterson, V. Sagan, and J. J. Sloan, "Deep learning-based water quality estimation and anomaly detection using Landsat-8/Sentinel-2 virtual constellation and cloud computing," *GISci. Remote Sens.*, vol. 57, no. 4, pp. 510–525, May 2020.

[25] H. Ding, L. Xu, Y. Wu, and W. Shi, "Classification of hyperspectral images by deep learning of spectral-spatial features," *Arabian J. Geosci.*, vol. 13, no. 12, pp. 635–646, Jun. 2020.

[26] G. Cheng, C. Yang, X. Yao, L. Guo, and J. Han, "When deep learning meets metric learning: Remote sensing image scene classification via learning discriminative CNNs," *IEEE Trans. Geosci. Remote Sens.*, vol. 56, no. 5, pp. 2811–2821, May 2018, doi: 10.1109/TGRS.2017.2783902.
[27] S. Liu, L. Xu, Q. Li, X. Zhao, and D. Li, "Fault diagnosis of water quality monitoring devices based on multiclass support vector machines and rule-based decision trees," *IEEE Access*, vol. 6, pp. 22184–22195, 2018, doi: 10.1109/ACCESS.2018.2800530.
[28] A. Vetrivel, M. Gerke, N. Kerle, F. Nex, and G. Vosselman, "Disaster damage detection through synergistic use of deep learning and 3D point cloud features derived from very high resolution oblique aerial images, and multiple-kernel-learning," *ISPRS J. Photogramm. Remote Sens.*, vol. 140, pp. 45–59, Jun. 2018.
[29] N. Kussul, M. Lavreniuk, S. Skakun, and A. Shelestov, "Deep learning classification of land cover and crop types using remote sensing data," *IEEE Geosci. Remote Sens. Lett.*, vol. 14, no. 5, pp. 778–782, May 2017.
[30] L. Ma, Y. Liu, X. Zhang, Y. Ye, G. Yin, and B. A. Johnson, "Deep learning in remote sensing applications: A meta-analysis and review," *ISPRS J. Photogramm. Remote Sens.*, vol. 152, pp. 166–177, Jun. 2019.
[31] Y. Bengio, P. Simard, and P. Frasconi, "Learning long-term dependencies with gradient descent is difficult," *IEEE Trans. Neural Netw.*, vol. 5, no. 2, pp. 157–166, Mar. 1994, doi: 10.1109/72.279181.
[32] S. Hochreiter and J. Schmidhuber, "Long short-term memory," *Neural Comput.*, vol. 9, no. 8, pp. 1735–1780, Nov. 1997, doi: 10.1162/neco.1997.9.8.1735.
[33] M. Pan, H. Zhou, J. Cao, Y. Liu, J. Hao, S. Li, and C.-H. Chen, "Water level prediction model based on GRU and CNN," *IEEE Access*, vol. 8, pp. 60090–60100, 2020, doi: 10.1109/ACCESS.2020.2982433.
[34] A. R. Slaughter, D. A. Hughes, D. C. H. Retief, and S. K. Mantel, "A management-oriented water quality model for data scarce catchments," *Environ. Model. Softw.*, vol. 97, pp. 93–111, Nov. 2017.
[35] G. Liu, Y. Li, H. Lyu, S. Wang, C. Du, and C. Huang, "An improved land target-based atmospheric correction method for lake taihu," *IEEE J. Sel. Topics Appl. Earth Observ. Remote Sens.*, vol. 9, no. 2, pp. 793–803, Feb. 2016, doi: 10.1109/JSTARS.2015.2503800.
[36] Y. Zhou, J. Luo, Z. Shen, X. Hu, and H. Yang, "Multiscale water body extraction in urban environments from satellite images," *IEEE J. Sel. Topics Appl. Earth Observ. Remote Sens.*, vol. 7, no. 10, pp. 4301–4312, Oct. 2014, doi: 10.1109/JSTARS.2014.2360436.
[37] S. K. McFeeters, "The use of the normalized difference water index (NDWI) in the delineation of open water features," *Int. J. Remote Sens.*, vol. 17, no. 7, pp. 1425–1432, May 1996.
[38] Y. Zhang, X. Liu, Y. Zhang, X. Ling, and X. Huang, "Automatic and unsupervised water body extraction based on spectral-spatial features using GF-1 satellite imagery," *IEEE Geosci. Remote Sens. Lett.*, vol. 16, no. 6, pp. 927–931, Jun. 2019, doi: 10.1109/LGRS.2018.2886422.
[39] Y. Wang, Z. Li, C. Zeng, G. Xia, and H. Shen, "An urban water extraction method combining deep learning and Google Earth engine," *IEEE J. Sel. Topics Appl. Earth Observ. Remote Sens.*, vol. 13, pp. 768–781, 2020, doi: 10.1109/JSTARS.2020.2971783.
[40] M. James McCracken, "Exploratory causal analysis with time series data," in *Exploratory Causal Analysis with Time Series Data*. San Rafael, CA, USA: Morgan & Claypool, 2016.
[41] L. James McClelland and C. David Plaut, "Computational approaches to cognition: Top-down approaches," *Current Opinion Neurobiol.*, vol. 3, no. 2, pp. 209–216, 1993, doi: 10.1016/0959-4388(93)90212-h.
[42] M. Li, W. Wu, B. Chen, L. Guan, and Y. Wu, "Water quality evaluation using back propagation artificial neural network based on self-adaptive particle swarm optimization algorithm and chaos theory," *Comput. Water, Energy, Environ. Eng.*, vol. 06, no. 03, pp. 229–242, 2017.
[43] V. Sagan, K. T. Peterson, M. Maimaitijiang, P. Sidike, J. Sloan, B. A. Greeling, S. Maalouf, and C. Adams, "Monitoring inland water quality using remote sensing: Potential and limitations of spectral indices, bio-optical simulations, machine learning, and cloud computing," *Earth-Science Rev.*, vol. 205, Apr. 2020, Art. no. 103187.
[44] L. Jin, S. Li, and B. Hu, "RNN models for dynamic matrix inversion: A control-theoretical perspective," *IEEE Trans. Ind. Informat.*, vol. 14, no. 1, pp. 189–199, Jan. 2018, doi: 10.1109/TII.2017.2717079.
[45] P. Liu, P. Zheng, and Z. Chen, "Deep learning with stacked denoising auto-encoder for short-term electric load forecasting," *Energies*, vol. 12, no. 12, p. 2445, Jun. 2019.

CHUHAN QI was born in Qiqihar, Heilongjiang, China, in 1996. She received the B.S. degree in electronics and information engineering from Heilongjiang University, in 2018, where she is currently pursuing the master's degree. Her main research interest includes remote sensing image processing.

SHUO HUANG was born in Harbin, Heilongjiang, China, in 1994. He received the B.S. degree in electronic information science and technology from Heilongjiang University, in 2017, where he is currently pursuing the master's degree. His main research interest includes remote sensing image processing.

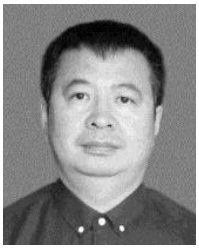

XIAOFEI WANG was born in Harbin, Heilongjiang, China, in 1977. He received the B.S. degree from the College of Environmental Science and Engineering and the College of Electronic Information and Optical Engineering, Nankai University, Tianjin, China, in 2001, and the M.S. and Ph.D. degrees in signal and information processing from the Harbin Institute of Technology (HIT), Harbin, in 2005 and 2011, respectively. He is currently an Associate Professor with the College of Electronic Engineering, Heilongjiang University. His research interests include hyperspectral data analysis and image processing, multisource information fusion, pattern recognition, and classification.